# Multi-wavelength study of extreme high-energy peaked BL Lac (EHBL) source 1ES 0229+200 using ultraviolet, X-ray and gamma-ray observations

Jyotishree Hota, <sup>1</sup> Rukaiya Khatoon, <sup>2</sup> Ranjeev Misra, <sup>3</sup> and Ananta C. Pradhan <sup>1</sup>

<sup>1</sup>Department of Physics and Astronomy, National Institute of Technology, Rourkela – 769008, India

<sup>2</sup>Centre for Space Research, North-West University, Potchefstroom – 2531, South Africa

<sup>3</sup>Inter-University Center for Astronomy and Astrophysics, Post Bag 4, Ganeshkhind, Pune – 411007, India

#### **ABSTRACT**

We present a comprehensive analysis of the broadband spectral energy distribution (SED) of the extreme highenergy peaked BL Lac (EHBL) source, 1ES 0229+200. Our study utilizes near-simultaneous data collected at various epochs between September 2017 and August 2021 (MJD: 58119-59365) from different instruments, including AstroSat-UVIT, SXT, LAXPC, Swift-UVOT, Fermi-LAT, and MAGIC. We investigate the one-zone synchrotron and synchrotron self-Compton (SSC) model, employing diverse particle distributions such as the log parabola, broken power law, power law with a maximum electron energy  $\gamma$ , energy-dependent diffusion (EDD), and energy-dependent acceleration (EDA) models to fit the broadband SED of the source. Our findings indicate that both peaks in the SED are well described by the one-zone SSC model across all particle distribution models. We estimate the jet power for different particle distributions. The estimated jet power for broken power law particle distributions is found to be on the order of 10<sup>47</sup> (10<sup>44</sup>) erg s<sup>-1</sup> for a minimum electron energy  $\gamma_{min} \sim 10 \ (10^4)$ . However, for intrinsically curved particle energy distributions (e.g., log parabola, EDD, and EDA models), the estimated jet power is  $\sim 10^{44}$  erg s<sup>-1</sup>. The SED fitting at five epochs enables us to explore the correlation between the derived spectral parameters of various particle distribution models. Notably, the observed correlations are inconsistent with the predictions in the power-law with a maximum  $\gamma$  model, although the EDD and EDA models yield the correlations as expected. Moreover, the estimated physical parameter values are consistent with the model assumptions.

*Keywords:* galaxies: active – BL Lacertae objects: general – BL Lacertae objects: individual: 1ES 0229+200 – acceleration of particles – diffusion – X-rays: galaxies

#### 1. INTRODUCTION

Blazars are a sub-class of active galactic nuclei (AGN) whose relativistic jet points in the direction of the observer's line of sight (Urry & Padovani 1995; Blandford et al. 2019). The key characteristics of blazars are their non-thermal broadband spectra, strong radio and optical polarization, and fast variability (Sambruna 2000; Fan et al. 2008). The spectral energy distribution (SED) of blazars shows a double bump that ranges from radio to very high energy (VHE)  $\gamma$ -ray (Fossati et al. 1998). According to the leptonic model, the first bump, which peaks in the optical to X-ray bands, is attributable to synchrotron emission while the second bump, which peaks in  $\gamma$ -ray energies, is explained by inverse Compton (IC) scatter-

Corresponding author: Jyotishree Hota hotajyoti@gmail.com, acp.phy@gmail.com

ing of low-energy photons (Urry & Mushotzky 1982; Ghisellini et al. 1985; Begelman et al. 1987; Blandford & Levinson 1995; Bloom & Marscher 1996; Sokolov et al. 2004).

The low-energy photons can be either synchrotron photons or photons that are external to the jet. When synchrotron photons serve as the target for IC scattering, it is called synchrotron self-Compton (SSC) (Jones et al. 1974; Maraschi et al. 1992; Ghisellini et al. 1993). On the other hand, the scattering of external photons is termed as the external-Compton process (Dermer et al. 1992; Sikora et al. 1994; B lażejowski et al. 2000; Shah et al. 2017). Furthermore, the high energy emission can be explained through hadronic processes such as the proton synchrotron process and pion production process (Mannheim & Biermann 1992; Mücke & Protheroe 2001).

Based on their spectral line in the optical bands, blazars are commonly classified into two types, such as flat spectrum radio quasars (FSRQs) and BL Lac objects. Further, depending upon their low-energy peak position, BL Lacs are categorized

into three groups: low-energy peak (LBL), intermediate energy peak (IBL), and high-energy peak (HBL) (Padovani & Giommi 1995).

In addition to the above classification, a new class of highenergy peak BL Lac sources, called extreme HBL (EHBL) sources, exhibit ambiguous spectral properties in high-energy emission. These sources show either a low-energy peak, a high-energy peak, or both, with peak frequencies surpassing 10<sup>17</sup> Hz for the synchrotron peak and above one TeV for the IC peak (Costamante, L. et al. 2001; Biteau et al. 2020). As predicted by the blazar sequence (Ghisellini & Tavecchio 2008; Ghisellini et al. 2017), these objects are located at the upper edge of the peak frequency and are at the lowest luminosity end. Over the last decade, the exceptional operational results of the Imaging Atmospheric Cherenkov Telescopes such as H.E.S.S., MAGIC, and VERITAS have identified 14 sources at VHE (E > 100 GeV) (Foffano et al. 2019; MAGIC Collaboration et al. 2019a). Among these sources, Costamante et al. (2018) and MAGIC Collaboration et al. (2019a) have detected seven objects in TeV energies and categorized them as hard-TeV blazars (high-energy peak located above one TeV) and the remaining seven EHBL sources are categorized as soft-TeV blazars by Foffano et al. (2019). Remarkably, it is noticed that two more sources, Mrk 501 and 1ES 1959+650, also show EHBL behaviour (hard-TeV spectra) during their flaring states (Pian et al. 1997; MAGIC Collaboration et al. 2018).

The EHBL source, 1ES 0229+200 (RA =  $38.202562^{\circ}$ , DEC: 20.28819°), is located at a considerable distance with a redshift of z = 0.14, (Woo et al. 2005; Aharonian et al. 2007a; Tavecchio et al. 2009)). This blazar is known for emitting VHE gamma rays in the hard TeV range (Aliu et al. 2014). Initially discovered during the Einstein IPC Slew Survey (Elvis et al. 1992), it was later identified as a highfrequency peaked BL Lac source based on the location of its synchrotron peak (Ackermann et al. 2011). H.E.S.S. detected the hard spectrum of this source in VHE emission, reaching up to 10 TeV, classifying it as a hard-TeV EHBL (Aharonian et al. 2007b). The source is also included in the third catalogue of Fermi-LAT, having been detected by Fermi-LAT after integrating four years of exposure time (Acero et al. 2015; Vovk et al. 2012). 1ES 0229+200 stands out as an ideal object for studying the extragalactic background light (EBL; Aharonian et al. 2007b; Kneiske & Dole 2010) and the intergalactic magnetic field (IGMF; Neronov & Vovk 2010; Tavecchio et al. 2010; Acciari et al. 2023) due to its distant and hard-spectrum nature as a blazar.

Modelling of hard-TeV spectra of a source is a challenging task. Various one-zone leptonic SSC models have been developed to explain the VHE emission of the source 1ES 0229+200 (Abdo et al. 2011; Aleksić et al. 2012; Aliu et al. 2014; Tanaka et al. 2014; Costamante et al. 2018; Foffano et al.

2019; Prandini et al. 2019; Diwan et al. 2023). Recently, a few more models have also been developed to explain the hard-TeV blazars. Zech & Lemoine (2021) developed a new onezone lepto-hadronic emission model for extreme-TeV blazars and showed that the acceleration in a single standing shock is capable of reproducing the jet emission. However, the re-acceleration on a second shock is required for the source like 1ES0229+200 (having hardest  $\gamma$ -ray spectra). Li et al. (2022) investigated the one-zone hadronuclear (pp) model and found that the hard-TeV spectrum of 1ES0229+200 is reproduced by the  $\gamma$ -ray emission from the  $\pi^0$  decay in the p-p interactions. A lepto-hadronic model proposed by Aguilar-Ruiz et al. (2022) suggests that the two-zone emission can reproduce the broadband SEDs of the hard-TeV blazars. The two-zone lepto-hadronic model was also able to relax several parameters required by the one-zone models.

To understand the hard-TeV systems, one has to find the energy-generating mechanism responsible for the high jet power  $(P_{jet})$  in such blazars. There are two mechanisms, Blandford-Znajek process (Blandford & Znajek 1977) and Blandford-Payne process (Blandford & Payne 1982), proposed for the jet formation in the hard-TeV blazars. The Blandford-Znajek model suggests that the blazar jet has an origin from a spinning black hole, and the  $P_{jet}$  is associated with the spin and mass of the black hole with the magnetic field at its horizon, whereas the Blandford-Payne model suggests that the jet is originated from the black hole accretion disk. A recent study by Zhang et al. (2022) suggests that the relativistic jets are probably dominated by the Blandford-Znajek process for both FSRQs and BL Lacs. The P<sub>iet</sub> estimation in the one-zone SSC model is primarily governed by the electron energy distribution in the blob, which is characterized mostly by the broken power law with a minimum electron Lorentz factor  $(\gamma_{min})$ . Xue et al. (2019) and Zech & Lemoine (2021) suggested a large  $\gamma_{min}$  value (~10<sup>4</sup>) is required to fit the SED in the TeV range spectra of the hard-TeV systems under one-zone SSC model. Zech & Lemoine (2021) proposed a standard one-zone lepto-hadronic emission model to study the broadband SED of TeV blazar 1ES 0229+200, and they calculated the total jet power  $P_{iet}$  in the order of  $\sim 10^{44}$  ergs/sec. Acciari et al. (2020) applied the single-zone SSC model, spine-layer model, and Proton-Synchrotron Scenario (PSS) to fit the spectra of various extreme blazars and estimated their total jet powers. The jet power calculated using the spine–jet scenario ( $10^{42} \text{ erg } sec^{-1}$ ) consistently appears more than one order of magnitude lower than those predicted by the SSC model ( $10^{44} \text{ erg } sec^{-1}$ ). In contrast, the  $P_{jet}$  estimated with the PSS is giving a higher value  $\sim 0.15 - 45.6 \times 10^{46} \text{ erg } sec^{-1}$  and this is because PSS requires a rather large power in the protons responsible for the emission, often larger than the Eddington luminosity of the black hole powering the AGN (Zdziarski & Bottcher 2015).

The  $P_{jet}$  estimates mentioned above are primarily derived by assuming that the underlying electron energy distribution follows either a broken power law or a single power law with an exponential cutoff (Acciari et al. 2020). Nonetheless, there is evidence that suggests the underlying electron distribution, which may resemble a log-parabola distribution, has a considerable curvature in the observed spectrum (Massaro et al. 2004; Tramacere et al. 2007). The curvature in the electron distribution is attributed to the energy dependency of particle acceleration/escape time-scales (Sinha et al. 2017; Goswami et al. 2018; Hota et al. 2021; Khatoon et al. 2022). Additionally, physically motivated models have been employed, including distributions where the curvature of the spectrum can be attributed to the energy dependency of the diffusion time-scale (EDD) or due to the energy dependency of the acceleration time-scale (EDA), or with a high energy cutoff attributable to radiative losses ( $\gamma$ -max models) (Hota et al. 2021; Khatoon et al. 2022).

This study presents a standard SSC model for the broadband spectra of the hard-TeV blazar 1ES 0229+200. Various electron energy distribution models, such as the broken power-law model, log-parabola model, power-law particle distribution with maximum electron energy (PL with  $\gamma_{max}$ ), energy-dependent diffusion (EDD), and energy-dependent acceleration (EDA) models, have been considered. These models have previously been verified for the X-ray spectral curvature of the HBL source, Mkn 421 (Hota et al. 2021; Khatoon et al. 2022). Furthermore, a study on the broadband emissions of a HBL source Mkn501 has been conducted (Bora et al. 2024).

We have applied these particle distribution models to investigate the hard-TeV blazar source, extending the model for a broadband SED analysis using various observations over five epochs in a wide energy range, from ultraviolet (UV; 0.01 KeV) to VHE  $\gamma$ -ray ( $\sim$ 10 TeV) bands.

The paper is organized as follows: In Section 2, we provide observations and data analysis procedure details. In Section 3, we present details of the  $\gamma$ -ray and VHE  $\gamma$ -ray analysis of the observed data. In Section 4, we discuss the broadband SED modelling of the source with synchrotron and SSC emission processes. The results are presented in Subsection 4.1 and 4.2. In Section 5, we summarized the results and their implications are discussed.

Throughout the paper, the following cosmological parameters are assumed:  $H_0 = 70 km \ s^{-1} \ Mpc^{-1}$ ,  $\Omega_M = 0.3$ ,  $\Omega_{\Lambda} = 0.7$ .

# 2. MULTI-WAVELENGTH OBSERVATIONS AND DATA ANALYSIS

AstroSat is the first multi-wavelength space observatory of India, carrying five major payloads with energies ranging from UV to hard X-ray (Agrawal 2006; Singh et al. 2014; Rao et al. 2016). AstroSat onboard instruments are

Ultra-Violet Imaging Telescope (UVIT: 130–300 nm; Tandon et al. 2017a,b), Soft X-ray focusing Telescope (SXT: 0.3–8.0 keV; Singh et al. 2017, 2016), Large Area X-ray Proportional Counter (LAXPC: 3–80 keV; Yadav et al. 2016), Cadmium Zinc Telluride Imager (CZTI: 10–100 keV; Rao et al. 2017) and Scanning Sky Monitor (SSM). SXT was the primary instrument used to observe the blazar, 1ES0229+200 at five different epochs between 2017 and 2022. LAXPC and UVIT were also used to observe the source simultaneously. The *AstroSat* observation details of the source are listed in Table 1. Furthermore, for the LAXPC and SXT observations conducted during August 8–12, 2021, no simultaneous UVIT observations are available. Hence, we have used UV data from Swift/ultraviolet optical telescope (UVOT) observations for the above duration.

In this study, we have used the quasi-simultaneous observations from UVIT and UVOT for UV data, SXT, and LAXPC for X-ray data, *Fermi*-LAT for  $\gamma$ -ray data, and VHE spectral data from the MAGIC observations (MAGIC Collaboration et al. 2019b, 2020). The details of the data reduction of UVIT, UVOT, SXT, LAXPC, and *Fermi*-LAT observations are as follows.

## 2.1. UVIT

UVIT is an imaging telescope onboard AstroSat consisting of three channels: FUV (1300 - 1800 Å), NUV (2000 - 3000 Å), and Visible (3200 - 5500 Å). The data reduction of the UVIT observations was performed with the software package CCDLAB (Postma & Leahy 2017). CCDLAB converts the Level 1 (L1) data into science-ready astronomical images. We extracted the L1 files of the UVIT observations and removed all the duplicate observations and short exposures (less than 120 seconds). The extracted L1 files were then supplied into CCDLAB for various corrections, viz., FPN, CPU distortion, flat-field, drift corrections, etc. The drift-corrected frames were then co-added to get the orbit-wise science-ready images for each observed filter. The images were co-aligned across all the orbits and merged into the final science images. Astrometric corrections were performed using the Gaia EDR3 catalogue. We applied the Source Extractor (SExtractor) tool (Bertin & Arnouts 1996) to extract the count rates in UVIT fits images corresponding to each filter. Then, the flux of the blazar source was calculated in all the UVIT filters using the unit conversion factor suggested by Tandon et al. (2017b). The flux values were then corrected for reddening using E(B-V) = 0.1192 values mentioned in Schlafly & Finkbeiner (2011).

### 2.2. *UVOT*

The UVOT (170-650 nm; Roming et al. 2005) onboard Swift uses three optical (U, B, V) and three UV (W1, M2, W2) filters to cover both the optical and UV portions of the

Table 1	Datails of the	A stro Cat observation	o with I AVDC CVT	and UVIT at five epochs.
Table I.	. Details of the	Astrosat observation	S WITH LAXPU. SX L	and UVII at five epochs.

Observation ID	Instrument	Energy	Observation date	Exposure	Count rate
		band		(ks)	(Count/sec)
	LAXPC20	3-30 keV	21-23, Sep 2017	57.4	$2.74 \pm 0.15$
A03_078T01_9000001546	SXT	0.7-7 keV	21-23, Sep 2017	57.4	$0.42 \pm 0.01$
	UVIT	FUVBaF2 (1541 Å)	22, Sep 2017	4.97	$0.168 \pm 0.007$
	UVIT	NUVB13(2447 Å)	22, Sep 2017	5.0	$0.463 \pm 0.01$
	LAXPC20	3-30 keV	9-10, Dec 2017	40	$2.99 \pm 0.10$
A04_130T01_9000001762	SXT	0.7-7 keV	9-10, Dec 2017	40	$0.40 \pm 0.02$
	UVIT	FUVBaF2 (1541 Å)	9, Dec 2017	4.97	$0.175 \pm 0.006$
	UVIT	NUVB13(2447 Å)	9, Dec 2017	4.97	$0.468 \pm 0.01$
	LAXPC20	3-30 keV	21-22, Dec 2017	50	$3.15\pm0.10$
A04_130T01_9000001792	SXT	0.7-7 keV	21-22, Dec 2017	50	$0.37 \pm 0.007$
	UVIT	FUVBaF2 (1541 Å)	21, Dec 2017	4.99	$0.168 \pm 0.006$
	UVIT	NUVB13 (2447 Å)	21, Dec 2017	5.0	$0.467 \pm 0.01$
	LAXPC20	3-30 keV	8-9, Dec 2018	57.4	$2.52 \pm 0.06$
A04_130T01_9000001822	SXT	0.7-7 keV	8-9, Jan 2018	57.4	$0.42 \pm 0.02$
	UVIT	FUVBaF2(1541 Å)	8, Jan 2018	4.9	$0.175 \pm 0.006$
	UVIT	NUVB13 (2447 Å)	8, Jan 2018	5	$0.50 \pm 0.01$
	LAXPC20	3-30 keV	8-12, Aug 2021	343.6	$2.32 \pm 0.09$
T04_034T01_9000004632	SXT	0.7-7 keV	8-12, Aug 2021	343.6	$0.24 \pm 0.006$
	UVOT	W1(2600 Å)	8-12, Aug 2021	3	$0.613 \pm 0.028$
	UVOT	W2(1928 Å)	8-12, Aug 2021	3	$0.440 \pm 0.021$
	UVOT	M2(2246 Å)	8-12, Aug 2021	3	$0.286 \pm 0.015$

spectrum. We have used Swift-UVOT observations to compliment the AstroSat SXT and LAXPC observations during 8–12 August, 2021 (at the fifth epoch) in the UV band. We have used observations in the W1, M2, and W2 filters of UVOT. We used the UVOTIMSUM command to combine all the observed images in each UVOT filter. The task UVOTSOURCE was used to extract the magnitudes from the combined images. The source and background regions were selected with radii 5" and 10", respectively, as input parameters in the UVOTSOURCE command. The observed magnitudes were then corrected for Galactic extinction using E(B-V) = 0.1192 mag and  $R_V = 3.1$  (Schlafly & Finkbeiner 2011). We converted the UVOT magnitudes to flux units using the photometric zero-points from Breeveld et al. (2011) and the conversion factors from Giommi et al. (2006).

## 2.3. *SXT*

SXT is a focusing telescope with a field of view (FOV) of around  $\sim 40'$  diameter and operates in the soft X-ray energy range of 0.3 – 8.0 keV for X-ray imaging and spectroscopy (Singh et al. 2017). The SXT observed 1ES 0229+200 in the Photon Counting (PC) mode for all the epoch and sxtpipeline<sup>1</sup> (AS1SXTLevel2, version 1.4b) was used to reduce the Level

1 data and obtain the cleaned Level 2 event files from different orbits. The standard Julia script developed by the instrument team was used to merge the cleaned event files from all orbits into a single file to avoid the problem of time-overlapping event files from successive orbits. The XSELECT (V2.4d) package built-in HEASOFT(V6.28) was used to extract the source spectrum from the processed Level-2 cleaned event files within a circular region of 15' centred on the source. An off-axis auxiliary response file (ARF) was generated by using the SXT ARF generation tool<sup>2</sup> with the help of the on-axis ARF (sxt\_pc\_excl00\_v04\_20190608.arf) as input. Further, we used "SkyBkg\_comb\_EL3p5\_Cl\_Rd16p0\_v01.pha" for a background spectrum and "sxt\_pc\_mat\_g0to12.rmf" for response matrix file (RMF; given by the SXT team). The SXT spectrum was re-binned using the GRPPHA tool. For the spectral analysis, we used the energy range between 0.5-7.0 keV. To modify the gain of the response file, the gainfit tool in XSPEC was used with a fixed slope of value one and the offset as a free parameter. To account for the Galactic absorption, we have utilized the TBabs model (Wilms et al. 2000) available in the XSPEC for the spectral fit. The equivalent hydrogen column density  $(N_H)$  was fixed at  $7.9 \times 10^{20}$  cm<sup>-2</sup> for

<sup>1</sup> http://www.tifr.res.in/~astrosat\_sxt/sxtpipeline.html

 $<sup>^2\,</sup>http://www.tifr.res.in/^{\sim}astrosat\_sxt/dataanalysis.html$ 

the X-ray observation, which was estimated from the online tool <sup>3</sup>, by the LAB survey group (Kalberla et al. 2005).

## 2.4. *LAXPC*

The LAXPC X-ray proportional counter has a high time resolution ( $\sim 10 \,\mu s$ ) and covers the energy range of 3–80 keV (Yadav et al. 2016; Antia et al. 2017; Agrawal et al. 2017; Misra et al. 2017). It comprises three identical co-aligned proportional counter units, named LAXPC 10, LAXPC 20, and LAXPC 30, with the effective area of each detector as  $\sim 2000 \ cm^2$ . All the Level 1 data were downloaded from the AstroSat archive. The Level 1 raw data were processed by the LAXPCSOFT package (version as of 2022 August 15; which is recommended by the instrument team and accessible at the website of the AstroSat Science Support Cell<sup>4</sup>). LAXPC command laxpc\_make\_event were used to merge different orbits. To avoid the Earth occultation and the South Atlantic Anomaly, good time intervals (GTI files) were created using the command laxpc\_make\_stdgti. Finally, the source and background spectra were extracted by using the command laxpc\_make\_spectra. We have adopted the faint source method to extract the background spectrum and lightcurve (Misra et al. 2021). Out of the three detectors, LAXPC 30 was switched off due to a gain instability issue arising from the gas leakage in the detector, and the LAXPC10 was working at low gain during the observation. Therefore, in our analysis, we have used only the LAXPC20 detector and limited the spectral analysis energy range to 4–18 keV.

#### 2.5. *FERMI*

The *Fermi* satellite carries the  $\gamma$ -ray instrument Large Area Telescope (LAT; Atwood et al. 2009), which is sensitive in the energy range 20 MeV to 300 GeV. The Fermi-LAT continuously monitored more than 5000 extragalactic  $\gamma$ -ray sources (4FGL; Abdollahi et al. 2020) between 2008 and 2018, out of which more than 3000 sources are blazars, suggesting that the  $\gamma$ -ray sky is heavily inhabited by relativistic jets. In this analysis, we have collected the Fermi-LAT data of the source, 1ES 0229+200 from 2008-08-04 (MJD54682.6) to 2022-10-30 (MJD 59882). The analysis was carried out in the energy band 100 MeV-300 GeV using the latest version of fermipy-v0.17.45 and fermitools1-v1.2.236. We selected a 15° region of interest (ROI) around the source to extract the photon events with evclass=128 and evtype=3, as recommended by the Fermi-LAT team in the fermitools documentation. The source model file was created using the Fermi 4FGL catalogue (Abdollahi et al. 2020), and the background

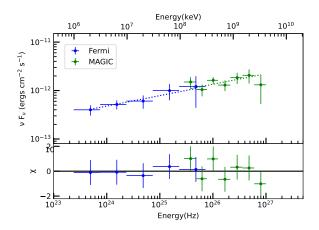


**Figure 1.** Spectral fitting with a simple power law model for the combined  $\gamma$ -ray (blue) and VHE  $\gamma$ -ray (green) data for 1ES 0229+200.

 $\gamma$ -ray emission and isotropic background emission were handled using "gll\_iem\_v07.fits" and "iso\_P8R3\_SOURCE\_V3\_v1.txt" files, respectively. Additionally, a 90° zenith angle was chosen to prevent contamination from the earth limb. While extracting within the ROI, the source parameters were left thawed while those outside were frozen to their 4FGL catalogue values. The test statistics (TS) defined as TS = 2logL, where L is the likelihood parameter of the analysis (Mattox et al. 1996) and is used to evaluate the detection significance of each source in the ROI.

#### 3. GAMMA-RAY ANALYSIS

This Section presents the  $\gamma$ -ray spectral analysis of 1ES 0229+200 using quasi-simultaneous observations from Fermi-LAT and MAGIC. EHBLs are generally considered relatively faint sources in the high-energy  $\gamma$ -ray domain, owing to their low average brightness and the shifts in the IC peak location at higher energies. The Fermi-LAT data considered in this work covers a substantial period from 2008 to 2022 (Section 2.5).

For the VHE  $\gamma$ -ray observations, we used the TeV spectra obtained from the MAGIC observations reported by MAGIC Collaboration et al. (2020), with a total exposure time of 117.46 hours and spanning a duration from 2013 to 2017. The VHE spectra has been corrected for extragalactic background light (EBL) absorption given by Franceschini et al. (2008).

We undertake a joint fitting of the two, using a simple power law and the best fit was found to be with an index  $\Gamma$  ~1.78±0.3 and the fit resulted in a  $\chi^2/dof = 4.28/10$ . The best-fit spectra with residuals are shown in Figure 1.

#### 4. SED MODELING

Broadband SED modelling of blazars is used to understand the underlying physical processes driving the broadband emission in both high-flux and low-flux states. We carried out broadband SED modelling of 1ES 0229+200 by using the data

<sup>3</sup> https://heasarc.gsfc.nasa.gov/cgi-bin/Tools/w3nh/w3nh.pl

<sup>4</sup> http://astrosat-ssc.iucaa.in

<sup>&</sup>lt;sup>5</sup> Fermipy webpage: https://fermipy.readthedocs.io/en/latest/

<sup>&</sup>lt;sup>6</sup> https://fermi.gsfc.nasa.gov/ssc/data/analysis/documentation/

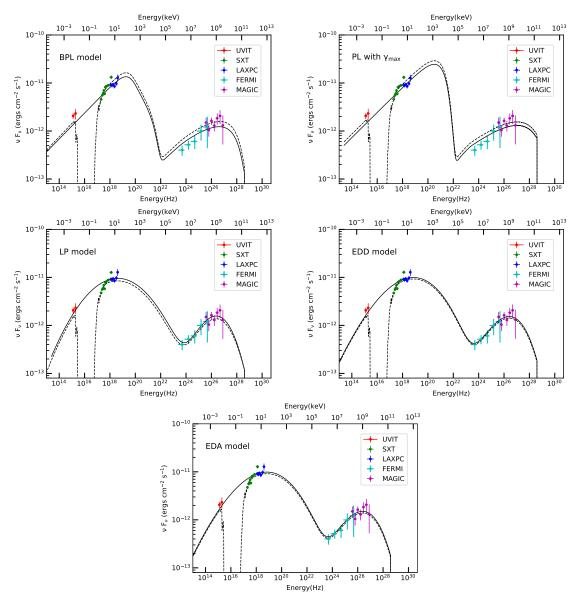


**Figure 2.** Broadband spectral energy distribution (SED) of 1ES 0229+200 for data sets of epoch-4. Different panels show the particle distribution models (mentioned at the top left corner of each plot) used to construct the SEDs. The solid lines represent the best-fit model without Galactic absorption. The dotted lines represent the best-fit model spectra for the SXT data with Galactic absorption.

from UV to VHE  $\gamma$ -ray bands. The time intervals selected for the broadband spectral study were determined based on the availability of simultaneous observations in UV and X-ray energies. We generated simultaneous multi-wavelength SEDs for all the five epochs of the observations of the source 1ES 0229+200 with AstroSat. Details of the observations from AstroSat instruments are provided in Table 1.

The one-zone SSC model provides an explanation for the broadband emission of EHBL sources like 1ES 0229+200. Leptonic models assume that interactions between relativistic electrons and the magnetic field in the emission zone produce the first hump of the SED in the energy range covering from radio to soft X-rays. Whereas the second hump of the SED is produced by IC scattering of a photon population, either the

synchrotron photons themselves (SSC) and/or the photon field external to the jet (EC). Based on SSC models (Ghisellini et al. 1993), synchrotron photons generated by relativistic electrons in the magnetic field will be up-scattered. We have employed a one-zone SSC leptonic model to explain the broadband SED fitting at each epoch. The model assumes a non-thermal emission from the blazar jet that arises from a spherical blob of radius R, filled with a tangled, homogeneous magnetic field (B), and isotropic electron distribution  $n(\gamma)$  moving with the relativistic velocity along the jet. The blazer jet is moving with a bulk Lorentz factor,  $\Gamma$ , at an angle  $\theta$  with respect to the observer's direction, affecting emission region by the beaming factor  $\delta = 1/\Gamma(1-\beta\cos\theta)$ .

If the electron Lorentz factor,  $\gamma$ , is represented in terms of  $\xi$  in such a way that  $\xi = \gamma \sqrt{\mathbb{C}}$ , where  $\mathbb{C} = 1.36 \times 10^{-11} \frac{\delta B}{1+z}$  with z being the redshift of source and  $\delta$  is the jet Doppler factor, the synchrotron flux that the observer receives at energy  $\epsilon$  will be (Begelman et al. 1984),

$$F_{\rm syn}(\epsilon) = \frac{\delta^3(1+z)}{d_L^2} V \, \mathbb{A} \int_{\xi_{min}}^{\xi_{max}} f(\epsilon/\xi^2) n(\xi) d\xi \qquad (1)$$

here, V is the volume of the emission region,  $d_L$  is the luminosity distance,  $\mathbb{A} = \frac{\sqrt{3}\pi e^3 B}{16m_e c^2\sqrt{c}}$  and f(x) is the synchrotron emissivity function (Rybicki & Lightman 1986). Rather than employing the electron's Lorentz factor,  $\gamma$ , the particle energy distribution is expressed by  $n(\xi)$ ). Note that  $\xi$  represents  $\gamma$ , and  $\xi^2$  has dimension of keV. Hota et al. (2021) solved Equation 1 numerically and included it as a local convolution model,  $synconv \otimes n(\xi)$  in XSPEC (Arnaud 1996). In this work, we have extended the numerical codes presented in Hota et al. (2021) to estimate the emissivities and to calculate the observed fluxes corresponding to the synchrotron and SSC emission processes. We have included it as a local convolution model,  $sscicon \otimes n(\xi)$  in XSPEC to fit the broadband SED of the source where  $n(\xi)$  is the particle distribution.

For this study, we utilize empirical models, such as log parabola (LP) and broken power law (BPL), and we input the particle distributions to the  $sscicon \otimes n(\xi)$  model. Additionally, we incorporate physical models, including power-law with maximum energy due to radiative cooling (PL with  $\gamma_{max}$ ), EDD, and EDA in order to fit the observed spectrum with the SSC emission. The goal of this analysis is to comprehensively explore and understand the observed spectrum through the application of both empirical and physical models.

 Log parabola (LP): The underlying particle distribution in this scenario is described as

$$n(\xi) = K(\xi/\xi_r)^{-\alpha - \beta \log(\xi/\xi_r)}$$
 (2)

here, particle spectral index is denoted as  $\alpha$  at the reference energy  $\xi^2 = \xi_r^2$ , the spectral curvature is represented by  $\beta$ , and K is the normalization of the particle density. The reference energy  $\xi_r^2$  kept constant at one keV throughout the spectral fit, whereas the parameters  $\alpha$ ,  $\beta$ , and norm K remained free.

• Broken power-law (BPL): This scenario of particle distribution is given by

$$n(\xi) = \begin{cases} K(\xi/1\sqrt{keV})^{-p} & \text{for } \xi < \xi_{break} \\ K\xi_{\text{break}}^{q-p}(\xi/1\sqrt{keV})^{-q} & \text{for } \xi > \xi_{break} \end{cases}$$
(3)

Where K represents the normalization, p and q represent the low and high energy photon indices, respectively,

while the Lorentz factor associated with the break energy is  $\xi_{break}$  and the transformation is represented by  $\xi = \gamma \sqrt{\mathbb{C}}$ . The distributions is non-zero for  $\xi_{min} < \xi < \xi_{max}$ , which correspond to  $\gamma_{min}$  and  $\gamma_{max}$  such that  $\xi_{min} = \gamma_{min} \sqrt{\mathbb{C}}$  and  $\xi_{max} = \gamma_{max} \sqrt{\mathbb{C}}$ .

• Power-law particle distribution with maximum electron energy (PL with  $\gamma_{max}$ ): In this case, we have considered that the particles accelerated by a shock, and then subsequently, these accelerated particles lose energy through radiative processes.

In such a case, the steady-state particle density is given by

$$\frac{\partial}{\partial \gamma} \left[ \left( \frac{\gamma}{\tau_{acc}} - \beta_s \gamma^2 \right) n_a \right] + \frac{n_a}{\tau_{esc}} = Q \delta(\gamma - \gamma_0) \tag{4}$$

where  $\tau_{acc}$  and  $\tau_{esc}$  represent the acceleration and escape time scales, respectively, and the radiative loss term includes  $\beta_s = \frac{4}{3} \frac{\sigma_T B^2}{8\pi m_e c}$ , B is the magnetic field,  $\sigma_T$  is the Thomson cross-section and  $m_e$  the electron mass. We consider that a mono-energetic injection of electrons Q at energy  $\gamma_0$ . The solution of the steady-state equation is described as

$$n(\xi) = K\xi^{-p} \left(1 - \frac{\xi}{\xi_{max}}\right)^{(p-2)}$$
 (5)

Where,  $K = Q_0 \tau_a \gamma_0^{p-1} \mathbb{C}^{p/2}$ ,  $p = \tau_{acc}/\tau_{esc} + 1$  is the particle spectral index,  $\xi_{max} = \gamma_{max} \sqrt{\mathbb{C}}$  with  $\gamma_{max} = 1/(\beta_s \tau_{acc})$  is the maximum Lorentz factor that an electron can attain before losing energy. The free parameters are,  $\xi_{max}$ , p, and the normalization  $\mathbb{N}$  defined as

$$\mathbb{N} = \frac{\delta^3(1+z)}{d_L^2} V \mathbb{A} Q_0 \tau_{acc} \gamma_0^{p-1} \mathbb{C}^{p/2}$$
 (6)

For  $\gamma_{max}$  model, the distribution is only for  $\xi > \xi_{min}$  such that  $\xi_{min} = \gamma_{min} \sqrt{\mathbb{C}}$ .

• Energy dependent diffusion model (EDD): In this case, we assume that the diffusion takes place in a region consisting of the tangled magnetic field, which may cause the diffusion coefficient dependent on the gyration radius. Consequently, escape time scale energy dependent or the diffusion coefficient energy is dependent as  $\tau_{esc}(\gamma)$  is given by  $\tau_{esc} = \tau_{esc,R} \left(\frac{\gamma}{\gamma_R}\right)^{-\kappa}$ . By ignoring the synchrotron energy loss and considering this escape time-scale dependence, the solution to Equation 4 will be (for detailed derivation see Hota et al. 2021; Khatoon et al. 2022)

$$n(\xi) = Q_o \tau_{acc} \sqrt{\mathbb{C}} \xi^{-1} \exp \left[ -\frac{\eta_{\rm R}}{\kappa} \left( \left( \frac{\xi}{\xi_{\rm R}} \right)^{\kappa} - \left( \frac{\xi_0}{\xi_{\rm R}} \right)^{\kappa} \right) \right]$$
 (7)

where  $\xi_R = \sqrt{\mathbb{C}}\gamma_R$ ,  $\xi_0 = \sqrt{\mathbb{C}}\gamma_0$  and  $\eta_R \equiv \tau_{acc}/\tau_{esc,R}$ .

**Table 2.** The best-fitted spectral parameter values of the log-parabola, broken power law, PL with  $\gamma_{max}$ , EDD, and EDA models. The broadband SED fitting for the various models is constructed using observations from UV to gamma rays at each epoch.

S.N.	Model	Unit	epoch-1	epoch-2	epoch-3	epoch-4	epoch-5	
	Parameters		21–23 Sep 17	9–10 Dec 17	21–22 Dec 17	8–9 Jan 18	8–12 Aug 21	
$log-parabola\ model\ (constant*redden*TBabs*eblcor*sscicon*log-parabola)$								
1	α	-	$2.40^{+0.02}_{-0.02}$	$2.65^{+0.02}_{-0.02}$	$2.59^{+0.02}_{-0.02}$	$2.67^{+0.02}_{-0.02}$	$2.44^{+0.02}_{-0.02}$	
2	β	-	$0.34^{+0.01}_{-0.01}$	$0.27^{+0.01}_{-0.01}$	$0.29^{+0.01}_{-0.01}$	$0.26^{+0.01}_{-0.01}$	$0.32^{+0.01}_{-0.01}$	
3	N	$(10^{-11})$	$2.39^{+0.2}_{-0.2}$	$1.50^{+0.2}_{-0.2}$	$1.63^{+0.1}_{-0.1}$	$1.42^{+0.2}_{-0.2}$	$1.99^{+0.2}_{-0.2}$	
4	B	$(10^{-3} \text{ G})$	$1.02^{+0.1}_{-0.1}$	$2.93^{+0.3}_{-0.3}$	$2.8^{+0.3}_{-0.3}$	$3.04^{+0.5}_{-0.5}$	$1.38^{+0.1}_{-0.1}$	
5	$log \ P_{jet}$		$43.9984^{+0.1}_{-0.1}$	$43.7553^{+0.1}_{-0.1}$	43.6735 <sup>+0.1</sup> <sub>-0.1</sub>	$43.7544^{+0.1}_{-0.1}$	$43.8437^{+0.1}_{-0.1}$	
6	$\chi^2(dof)$	-	407.2(240)	86.5(88)	138.8(107)	105(106)	151.3(94)	
7	$factor_{sxt}$	-	$0.83^{+0.04}_{-0.04}$	$0.76^{+0.02}_{-0.02}$	$0.75^{+0.02}_{-0.02}$	$0.88^{+0.04}_{-0.04}$	$0.63^{+0.03}_{-0.03}$	
	Broker	n power law i	model (constan	t * redden * TB	Babs * eblcor * s	scicon * bknp	<i>o</i> )	
1	γmin		10	10	10	10	10	
2	$\gamma_{max}$		108	108	108	108	10 <sup>8</sup>	
3	ξbreak	$\sqrt{keV}$	> 10.5	> 6.3	> 10.5	> 7.8	> 5.4	
4	p	-	$2.25^{+0.03}_{-0.03}$	$2.46^{+0.03}_{-0.03}$	$2.40^{+0.03}_{-0.03}$	$2.55^{+0.03}_{-0.03}$	$2.32^{+0.01}_{-0.01}$	
5	q	-	4.0	4.0	4.0	4.0	4.0	
6	N	$(10^{-12})$	$11.5^{+0.8}_{-0.8}$	$09.10^{+0.6}_{-0.6}$	$10.02^{+0.7}_{-0.7}$	$8.68^{+0.7}_{-0.7}$	$10.7^{+0.9}_{-0.9}$	
7	В	$(10^{-3} \text{ G})$	$1.67^{+0.3}_{-0.3}$	$3.12^{+0.3}_{-0.3}$	$2.58^{+0.3}_{-0.3}$	$3.40^{+0.3}_{-0.3}$	$1.97^{+0.3}_{-0.3}$	
8	$log P_{jet}$		$46.0214_{0.06}^{0.06}$	45.4643 <sup>0.01</sup> <sub>0.01</sub>	$46.5954_{0.01}^{0.01}$	$46.69_{0.01}^{0.01}$	$46.21_{0.008}^{0.008}$	
9	$\chi^2(dof)$	-	310(243)	84.8(89)	110.2(108)	102.3(107)	112.4(95)	
10	$factor_{sxt}$	-	$1.1^{+0.06}_{-0.06}$	$0.98^{+0.06}_{-0.06}$	$0.90^{+0.06}_{-0.06}$	$1.2^{+0.09}_{-0.09}$	$0.81^{+0.04}_{-0.04}$	

**Table 2.** (Continued...) The best-fitted spectral parameter values of the log-parabola, broken power law, PL with  $\gamma_{max}$ , EDD, and EDA models. The broadband SED fitting for the various models is constructed using observations from UV to gamma rays at each epoch.

S.N.	Model	Unit	epoch-1	epoch-2	epoch-3	epoch-4	epoch-5		
	Parameters		21–23 sep 17	9–10 dec 17	21–22 dec 17	8–9 jan 18	8–12 aug 21		
PL with $\gamma_{max}$ model (constant * redden * TBabs * eblcor * sscicon * $\gamma_{max}$ )									
1	p	-	$2.25^{+0.03}_{-0.03}$	$2.51^{+0.01}_{-0.05}$	$2.42^{+0.02}_{-0.09}$	$2.53^{+0.01}_{-0.05}$	$2.30^{+0.03}_{-0.03}$		
2	$\xi_{max}$	-	> 23	> 17	> 31.5	> 8.8	> 13		
3	N	$10^{-12}$	$11.6^{+0.9}_{-0.9}$	$09.01^{+0.24}_{-0.7}$	$9.40^{+0.7}_{-0.7}$	$8.60^{+0.6}_{-0.6}$	$11.3^{+0.8}_{-0.8}$		
4	В	$10^{-3}$ G	$1.56^{+0.4}_{-0.4}$	$4.14^{+0.6}_{-0.5}$	$3.68^{+0.6}_{-0.5}$	$4.23^{+0.5}_{-0.5}$	$1.70^{+0.2}_{-0.2}$		
5	$log P_{jet}$		$47.30^{+0.062}_{-0.062}$	$45.46_{0.067}^{0.067}$	$48.07_{0.069}^{0.069}$	$45.49_{0.07}^{0.07}$	$45.15_{0.07}^{0.07}$		
6	$\chi^2(dof)$	-	307.8(243)	82.5(89)	108.2(108)	101.2(107)	111.8(96)		
7	$factor_{sxt}$	-	$1.1^{+0.05}_{-0.05}$	$1.01^{+0.05}_{-0.05}$	$0.93^{+0.05}_{-0.05}$	$1.1^{+0.05}_{-0.05}$	$0.83^{+0.05}_{-0.05}$		
EDD model (constant * redden * TBabs * eblcor * sscicon * edd)									
1	В	10 <sup>-3</sup> G	1.26+0.1	1.44+0.3	2.80+0.3 -0.3	3.05+0.5	$1.27^{+0.1}_{-0.1}$		
2	$\psi$		$1.30^{+0.02}_{-0.02}$	$1.39^{+0.02}_{-0.02}$	$1.53^{+0.04}_{-0.04}$	$1.61^{+0.06}_{-0.06}$	$1.37^{+0.03}_{-0.03}$		
3	К		$0.157^{+0.004}_{-0.004}$	$0.144^{+0.004}_{-0.004}$	$0.128^{+0.003}_{-0.003}$	$0.120^{+0.003}_{-0.003}$	$0.146^{+0.004}_{-0.004}$		
4	N	$10^{-8}$	$7.49^{+1.0}_{-1.0}$	$24.70^{+8.0}_{-8.0}$	$209.0^{+50.0}_{-50.0}$	$897.3^{+200.0}_{-200.0}$	$20.06^{+5.0}_{-5.0}$		
5	$log P_{jet}$		$44.1847^{+0.007}_{-0.007}$	$44.3757^{+0.01}_{-0.01}$	$44.6721^{+0.1}_{-0.1}$	$44.9290^{+0.1}_{-0.1}$	$44.3367^{+0.008}_{-0.008}$		
6	$\chi^2(dof)$		365(242)	80.6(85)	130.5(107)	101.5(106)	137.0(95)		
7	$factor_{sxt}$		$0.93^{+0.04}_{-0.04}$	$0.94^{+0.06}_{-0.06}$	$0.74^{+0.04}_{-0.04}$	$0.93^{+0.04}_{-0.04}$	$0.68^{+0.04}_{-0.04}$		
		EDA mo	odel (constant * i	redden * TBabs	* eblcor * ssci	con * eda)			
1	В	10 <sup>-3</sup> G	1.26 <sup>+0.1</sup> <sub>-0.1</sub>	1.28+0.1	2.75 <sup>+0.2</sup> <sub>-0.2</sub>	3.15 <sup>+0.2</sup> <sub>-0.2</sub>	1.24 <sup>+0.1</sup> <sub>-0.1</sub>		
2	К		$0.144^{+0.004}_{-0.004}$	$0.132^{+0.004}_{-0.004}$	$0.120^{+0.005}_{-0.005}$	$0.111^{+0.003}_{-0.003}$	$0.135^{+0.004}_{-0.004}$		
3	$\psi$		$1.46^{+0.03}_{-0.03}$	$1.53^{+0.02}_{-0.02}$	$1.65^{+0.04}_{-0.04}$	$1.74^{+0.06}_{-0.06}$	$1.50^{+0.03}_{-0.03}$		
4	N	$10^{-7}$	$4.47^{+0.9}_{-0.9}$	$16.90^{+7.0}_{-7.0}$	$130.0^{+40.00}_{-40.00}$	814.0 <sup>+200.00</sup> <sub>-200.00</sub>	$11.30^{+5.0}_{-5.0}$		

**Notes**: For broadband analysis, the size of the emission region we have considered is  $R = 10^{17}$  cm and bulk Lorentz factor  $\Gamma = 20$ . Jet Power  $P_{jet}$  is in logarithmic scale with the units of erg  $s^{-1}$ .

**Table 2.** (Continued...) The best-fitted spectral parameter values of the log-parabola, broken power law, PL with  $\gamma_{max}$ , EDD, and EDA models. The broadband SED fitting for the various models is constructed using observations from UV to gamma rays at each epoch.

S.N.	Model	Unit	epoch-1	epoch-2	epoch-3	epoch-4	epoch-5
	Parameters		21-23 Sep 17	9–10 Dec 17	21–22 Dec 17	8–9 Jan 18	8–12 Aug 21
5	log P <sub>jet</sub>		44.1053 <sup>+0.007</sup> <sub>-0.007</sub>	$44.0360^{+0.01}_{-0.01}$	$44.5188^{+0.01}_{-0.01}$	$44.8804^{+0.01}_{-0.01}$	$44.23^{+0.008}_{-0.008}$
6	$\chi^2(dof)$		367(242)	82.3(88)	131(107)	101.7(106)	137.8(95)
7	$factor_{sxt}$		$0.92^{+0.04}_{-0.04}$	$0.94^{+0.06}_{-0.06}$	$0.74^{+0.04}_{-0.04}$	$0.93^{+0.04}_{-0.04}$	$0.67^{+0.04}_{-0.04}$

**Notes**: For broadband analysis, the size of the emission region we have considered is  $R = 10^{17}$  cm and bulk Lorentz factor,  $\Gamma = 20$ . Jet Power  $P_{jet}$  is in logarithmic scale with the units of erg  $s^{-1}$ .  $factor_{sxt}$  is the relative cross-normalization constant between X-ray instrument SXT and LAXPC. This factor was kept frozen at 1 for LAXPC, whereas it was kept free for the SXT instrument.

After removing the degenerate parameters, we can use the updated Equation as follows

$$n(\xi) = K' \xi^{-1} \exp\left[-\frac{\psi}{\kappa} \, \xi^{\kappa}\right] \tag{8}$$

where  $\psi = \eta_R \left( \mathbb{C} \gamma_R^2 \right)^{-\kappa/2} = \eta_R \xi_R^{-\kappa}$ , and the normalization parameter (K') is given as

$$K' = Q_0 \tau_{acc} \sqrt{\mathbb{C}} \exp \left[ \frac{\eta_{\rm R}}{\kappa} \left( \frac{\gamma_0}{\gamma_{\rm R}} \right)^{\kappa} \right]$$
 (9)

and further modified into  $\mathbb{N}$  as

$$\mathbb{N} = \frac{\delta^3 (1+z)}{d_I^2} V \mathbb{A} K' \tag{10}$$

We have considered  $\psi$ ,  $\kappa$ , and  $\mathbb N$  as the free parameters for the above model.

• Energy dependent acceleration model (EDA): We next consider a case where the energy dependence of acceleration time scale as  $\tau_{acc} = \tau_{acc,R} \left(\frac{\gamma}{\gamma_R}\right)^K$ . So considering the above dependency  $\tau_{acc}$ , the solution to Equation 4 will be (defined in Hota et al. 2021; Khatoon et al. 2022)

$$n(\xi) = Q_0 \tau_{acc,R} \sqrt{\mathbb{C}} \xi_R^{-\kappa} \xi^{\kappa-1} \exp \left[ -\frac{\eta_R}{\kappa} \left( \left( \frac{\xi}{\xi_R} \right)^{\kappa} - \left( \frac{\xi_0}{\xi_R} \right)^{\kappa} \right) \right]$$
(11)

where  $\xi_0 = \sqrt{\mathbb{C}}\gamma_0$ ,  $\xi_R = \sqrt{\mathbb{C}}\gamma_R$  and  $\eta_R \equiv \tau_{acc,R}/\tau_{esc}$ .

We can recast the distribution as

$$n(\xi) = K' \xi^{\kappa - 1} \exp\left[-\frac{\psi}{\kappa} \, \xi^{\kappa}\right] \tag{12}$$

where  $\psi = \eta_R \left(\mathbb{C}\gamma_R^2\right)^{-\kappa/2} = \eta_R \xi_R^{-\kappa}$ , and the normalization (K') is defined in Equation 13 and further modified as  $\mathbb{N}$  (Equation 14).

$$K' = Q_0 \tau_{acc, R} \sqrt{\mathbb{C}} \xi_R^{-\kappa} \exp \left[ \frac{\eta_R}{\kappa} \left( \frac{\xi_0}{\xi_R} \right)^{\kappa} \right]$$
 (13)

$$\mathbb{N} = \frac{\delta^3 (1+z)}{d_x^2} V \, \mathbb{A} K' \tag{14}$$

We have considered  $\psi$ ,  $\kappa$ , and  $\mathbb N$  as the free parameters for the above model.

To consider Galactic absorption while fitting the broadband SED of the source, we used the TBabs model (Wilms et al. 2000) available in the XSPEC with the equivalent hydrogen column density ( $N_H$ ) set at  $7.9 \times 10^{20} \text{cm}^{-2}$  as determined by the online tool<sup>7</sup> created by the LAB survey group (Kalberla et al. 2005).

For the SED spectral fitting, we fixed the size R, the bulk Lorentz factor  $\Gamma$ , and the opening angle  $\theta$ , at  $10^{17}$  cm, 20, and  $0^{\circ}$ , respectively, while keeping other parameters free. However, we have discussed later the impact of variations of these parameters. For the broken power-law model, we further fix the minimum and maximum Lorentz factors,  $\gamma_{min}$  and  $\gamma_{max}$  to 10 and  $10^{8}$ , respectively. The best-fit parameters with errors are listed in Table 2 along with  $\chi^{2}$  for each of the epochs and different particle distributions. Figure 2 shows the model along with the data for a representative epoch. The solid lines in Figure 2 represent the best-fit model without Galactic absorption. The dotted lines represent the best-fit

<sup>&</sup>lt;sup>7</sup> https://heasarc.gsfc.nasa.gov/cgi-bin/Tools/w3nh/w3nh.pl

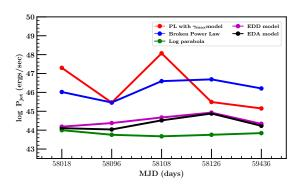


**Figure 3.** Jet power estimated for all five models as indicated in the legend at five different epochs.

model spectra for the SXT data with Galactic absorption. Note that to take into account the calibration uncertainties between LAXPC and SXT instruments a constant factor has been multiplied to the SXT model, which causes the dotted lines to be shifted compared to the solid ones. The constant factor was fixed for LAXPC, whereas it was free to vary for the SXT ( $factor_{sxt}$ ) instrument. The constant factor for SXT ( $factor_{sxt}$ ) for each of the epochs is listed in Table 2.

## 4.1. Jet Power

We have calculated the total jet power  $(P_{jet})$ , or the total power carried by electrons, Poynting flux, radiation, and protons (Celotti & Ghisellini 2008) using Equation 15 as given below,

$$P_{iet} = 2 \pi^2 R^2 \Gamma^2 \beta_c u_b'$$
 (15)

Here, factor 2 refers to two-sided jets,  $\Gamma$  represents the bulk Lorentz factor, R is the size of the emission region, and  $u'_k$  are the energy densities in the co-moving jet's frame of the magnetic field (k = mag), relativistic electrons (k = ele), and cold protons (k = kin).

We have calculated the  $P_{jet}$  values for all the five particle distribution models used for the broadband SED fitting described in Section 4. Since we have performed SED fitting by freezing R and  $\Gamma$  values at  $10^{17}$  cm and 20, respectively,  $P_{jet}$  values are calculated for the fixed R and  $\Gamma$  for all the particle distribution models and at all the five epoch observations, given in Table 2. In Figure 3, we present the variation of jet power at different epochs for all the models. The maximum jet power values are obtained for the PL with  $\gamma_{max}$  model and the broken power law model i.e., approximately two orders of magnitude higher compared to the log parabola, EDD, and EDA models. Notably, the values of jet power remain nearly constant for the log parabola, EDD, and EDA models, while for the broken power law and PL with  $\gamma_{max}$  models, the jet power values exhibit variability across all five epochs.

Furthermore, to examine the variation in the jet power of the blazar source 1ES 0229+200 at different values of  $\Gamma$  and R, we calculated the jet power by systematically varying  $\Gamma$  and

R for both the log parabola and broken power law models. The top left panel of Figure 4 illustrates the variation of  $\Gamma$  with  $\chi^2$  (top) and jet power (bottom). The jet power shows a slight increase (by a factor of one or two) as the  $\Gamma$  values vary from 10 to 35, becoming approximately constant at  $\Gamma \geq 35$ . In the top right panel of Figure 4, the variation of R with its respective  $\chi^2$  (top) and jet power (bottom) values is depicted. The plot indicates a slight decrease (by a factor of 2(1)) in jet power for the log parabola model (broken power law), and the  $\chi^2$  remains stable with decreasing R values. However,  $\chi^2$  values increases below R =  $10^{15}$  ( $10^{16}$ ) for the broken power-law (log parabola model). Therefore, the general  $P_{jet}$  estimates with  $\Gamma = 20$  and size R =  $10^{17}$  cm are insensitive to their presumptions.

Additionally, the bottom panel of Figure 4 displays the variation in jet power (bottom) and  $\chi^2$  (top) of the source 1ES 0229+200 with respect to  $\gamma_{min}$  for the broken power-law particle distribution. The jet power decreases with increasing  $\gamma_{min}$  for large values, while the  $\chi^2$  remains constant up to  $10^4$  and increases beyond that threshold. We find that the  $P_{jet}$  for the broken power-law model is  $\sim 10^{44}$  ergs/sec for a value as large as  $\gamma_{min} = 10^4$ .

### 4.2. Correlation study of spectral parameter

The study of correlation among various spectral parameters is important to understand the dependence between the fit parameters and the observed properties. We obtained spectral parameters for log-parabola, Broken power law, PL with  $\gamma_{max}$ , EDD, and EDA models. Then, we determined Spearman's rank correlation coefficient  $(r_s)$  and null hypothesis probability  $(P_{rs})$  for all the derived parameters in each model.

The scatter plots between spectral parameters of the logparabola are shown in Figure 5. A significant anti-correlation is observed between fit parameters,  $\alpha$  vs.  $\beta$  and normalization each with  $r_s = -0.99$  ( $P_{rs} = 1.4 \times 10^{-24}$ ). A positive correlation is found between  $\beta$  vs. normalization and  $\alpha$  vs. B, each with  $r_s = 0.99$  ( $P_{rs} = 1.4 \times 10^{-24}$ ). Furthermore, a significant anti-correlation is observed between fit parameter magnetic field vs.  $\beta$  and normalisation, each having  $r_s = -0.99$  ( $P_{rs} = 1.4 \times 10^{-24}$ ).

The scatter plots for the broken power law model parameters are presented in Figure 6. A strong anti-correlation is observed between index 'p' vs. normalization and the magnetic field 'B' vs. normalization, both with  $r_s = -0.99$  ( $P_{rs} = 1.4 \times 10^{-24}$ ). On the contrary, a strong positive correlation is found between index p and magnetic field B with  $r_s = 0.99$  ( $P_{rs} = 1.4 \times 10^{-24}$ ).

Figure 7 illustrates the scatter plot for the PL with  $\gamma_{max}$  model parameters. A pronounced anti-correlation is noted in both index 'p' vs. normalization and magnetic field 'B' vs. normalization, each with  $r_s = -0.99$  ( $P_{rs} = 1.4 \times 10^{-24}$ ). The observed strong anti-correlation between index p and

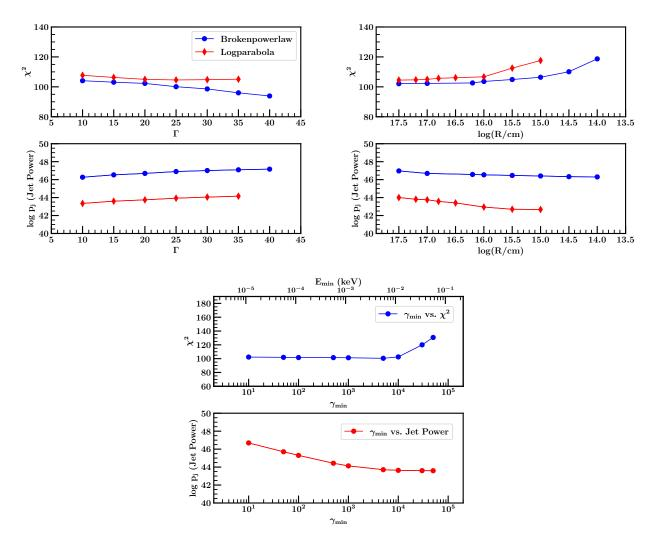


Figure 4. Top left panel represents the variation of  $\Gamma$  with  $\chi^2$  and  $P_{jet}$  whereas the top right panel represents the variation of size of the region (R) with  $\chi^2$  and  $P_{jet}$  for both the Broken power law (blue) and Log parabola (red) models for data epoch-4. The bottom panel shows the variation of  $\gamma_{min}$  with  $\chi^2$  and  $P_{jet}$  only for the Broken power law model.

normalization contradicts the theoretical form of  $\mathbb{N}$  ( $log\mathbb{N} \propto p$ ; Equation 6). Additionally, a strong positive correlation is also noted between index 'p' and the magnetic field; however, this conflicts with the theoretical relation,  $\mathbf{B} \propto (p-1)^{-1/n}$  (Khatoon et al. 2022), which predicts a negative correlation between 'p' and 'B'.

Figure 8 shows the scatter plot between EDD model fit parameters. It is expected that  $\log_{10}(\psi)$  will be inversely and linearly proportional to  $\kappa$  since  $\psi = \eta_R \xi_R^{-\kappa}$ , and as expected we found a strong anti-correlation in  $\psi$  vs  $\kappa$ .

The above equation can be further expressed as

$$\log_{10}(\psi) = \log_{10}(\eta_R) - \kappa \times \log_{10}(\xi_R)$$
 (16)

Equation 16 was fitted using the values of  $\kappa$  and  $\psi$  obtained from the broadband SED fitting. The fitted line in the left panel of Figure 8 on the  $\kappa$  vs.  $\log_{10}(\psi)$  plot is having a slope

 $(\log_{10}(\xi_R))$  of 2.54 and an intercept  $(\log_{10}(\eta_R))$  of 0.51. This implies that the observed photon energy  $\xi_R^2 = 122$  MeV falls within the spectral coverage of our broadband spectra. We can estimate the  $\gamma_R$   $(\xi_R/\sqrt{\mathbb{C}})$  and  $\eta_R$  to be  $3.6 \times 10^8$  and 3.24, respectively.

Additionally, injection energy can be estimated using the correlation between the best-fit parameters,  $\kappa$  and  $\mathbb{N}$ . The relation between  $\kappa$  and  $\mathbb{N}$  is given in Equation 10 which can be further expressed as

$$\ln(\mathbb{N}) = \frac{\eta_R}{\kappa} A^{\kappa} + B \tag{17}$$

Equation 17 was fitted with the  $\kappa$  and  $\mathbb{N}$  values obtained from the broadband SED fitting.

Using  $\eta_R = 3.24$  from above, we fitted the  $\kappa$  vs.  $\ln(\mathbb{N})$  plot shown in Figure 8, to obtain  $A = 9.66 \times 10^{-04}$ , B = -23.4. Since,  $\gamma_0 \sim A\gamma_R$ , we can estimate the injection energy,  $\gamma_0$ 

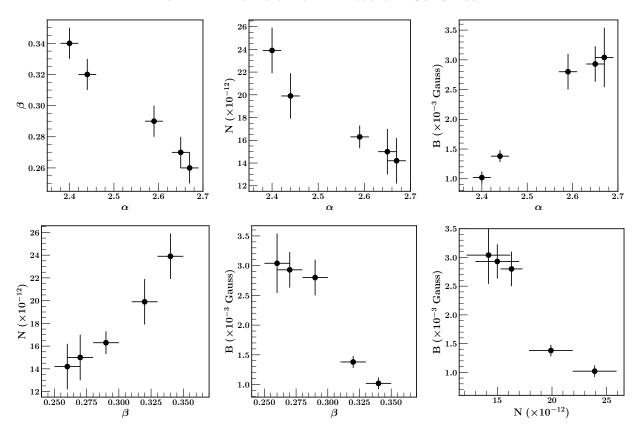


**Figure 5.** Scatter plots between the derived parameters obtained for log parabola model at five epochs. Top left panel:  $\alpha$  vs.  $\beta$ , top middle panel: normalisation vs.  $\alpha$ , top right panel:  $\alpha$  vs. magnetic field value, bottom left panel:  $\beta$  vs. normalisation, bottom middle panel:  $\beta$  vs. magnetic field, and bottom right panel: normalisation vs. magnetic field.

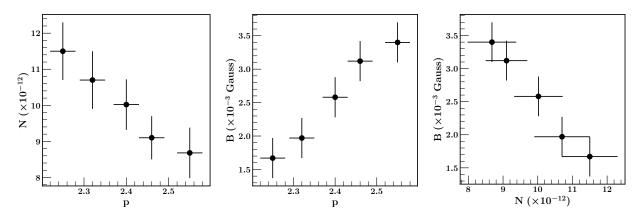


Figure 6. Scatter plots between the derived parameters with broken power law model at five epochs. Left panel: p vs. normalisation, middle panel: p vs. magnetic field, and right panel: normalisation vs. magnetic field.

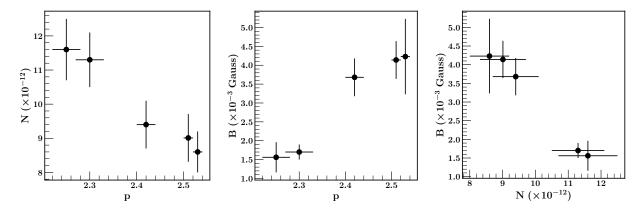
 $\sim 3.5 \times 10^5$ , which is significantly smaller than  $\gamma_R$ . Such a high value of minimum Lorentz factor with a standard one-zone SSC model for EHBLs sources has also been reported by several authors (Kaufmann et al. 2011; Zech & Lemoine 2021; Goswami et al. 2024).

Figure 9 shows the scatter plot between the EDA model fit parameters. The free parameters  $\kappa$ ,  $\psi$ , and  $\mathbb{N}$  in the EDA model are similar to the EDD model. The  $\kappa$  and  $\psi$  parameters

of the EDA model follow a similar trend as in Equation 16. However, the  $\kappa$  and  $\mathbb N$  parameters of the EDA model have a relation given in Equation 14 which can be further expressed as

$$\ln(\mathbb{N}) = \frac{\eta_R}{\kappa} A^{\kappa} - \kappa \ln(\xi_R) + B \tag{18}$$

We fitted both Equation 16 and Equation 18 with the  $\kappa$ ,  $\psi$ , and  $\mathbb N$  values of the EDA model. Equation 17 was applied to the  $\kappa$  vs.  $\log_{10}(\psi)$  plot (left panel of Figure 9), while



**Figure 7.** Scatter plots between the derived parameters with PL with  $\gamma_{max}$  model at five epochs. Left panel: p vs. normalisation, middle panel: p vs. magnetic field, and right panel: normalisation vs. magnetic field.

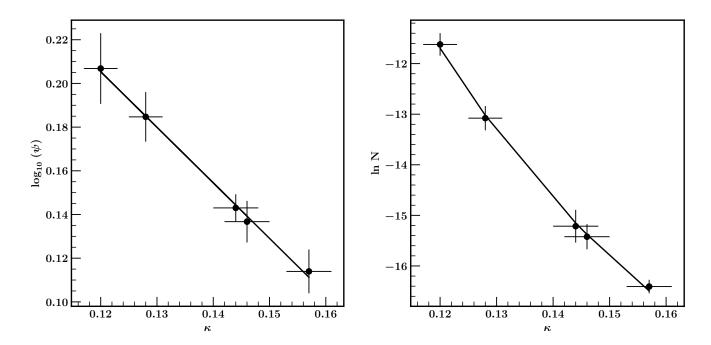


**Figure 8.** Scatter plots between the free parameters of the EDD model at five epochs. Left panel:  $\kappa$  vs.  $\log_{10} \psi$ ; right panel:  $\ln N$  vs.  $\kappa$ . A solid curve in each panel is the best-fitted function as described in the text.

Equation 18 was applied to the  $\kappa$  vs.  $\ln(\mathbb{N})$  (right panel of Figure 9). From the fitted equations of the EDA model, we obtained  $\xi_R^2 = 66$  MeV,  $\gamma_R = 2.66 \times 10^8$ ,  $\eta_R = 3.21$ ,  $A = 7.5 \times 10^{-04}$ , and B = -21.8. With the relation,  $\gamma_0 \sim 7.5 \times 10^{-04} \gamma_R$ , we find  $\gamma_0 = 2 \times 10^5$ . Thus the results obtained from the EDA model are qualitatively similar to those obtained for the EDD model.

#### 5. SUMMARY AND DISCUSSION

In this work, we have performed a detailed broadband SED analysis of an EHBL source, 1ES 0229+200, using simultaneous multi-wavelength observation taken at different epochs from September 2017 to August 2021 (MJD 58119-59365)

using *AstroSat*–LAXPC, SXT, and UVIT. We have also included the  $\gamma$ -ray data from *Fermi*-LAT observed from August 2008 to October 2022 (MJD 54682.6–59882) and VHE  $\gamma$ -rays data of MAGIC observed from 2013 to 2017 (MJD 56293 – 58118). We used the one-zone synchrotron and SSC model ( $sscicon \otimes n(\xi)$ ) with various particle distributions viz. log parabola, broken power law, power law with maximum gamma ( $\gamma_{max}$ ), energy-dependent diffusion (EDD) and energy-dependent acceleration (EDA) model to fit the broadband SED.

According to Costamante et al. (2018), the broadband SED modelling in hard-TeV blazars can be explained by the one-zone SSC model with a smooth broken power-law particle

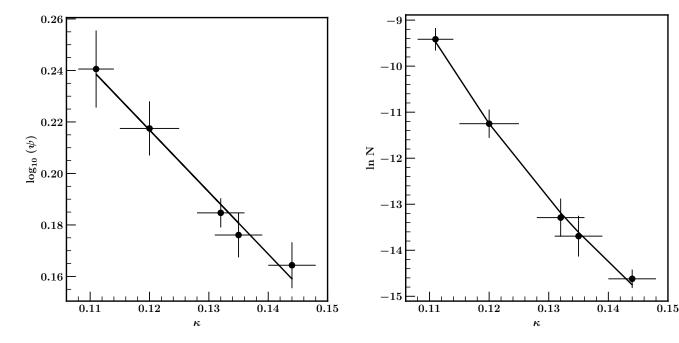


**Figure 9.** Scatter plots between the free parameters of the EDA model at five epochs. Left panel:  $\kappa$  vs.  $\log_{10} \psi$ ; right panel:  $\ln N$  vs.  $\kappa$ . A solid curve in each panel is the best-fitted function as described in the text.

distribution. They estimated the break energy of the electrons,  $\gamma_{break} \sim 10^6$  and magnetic field strengths in the range of a few mG for six hard-TeV blazars. In this work, for the TeV blazar 1ES 0229+200, we also find the magnetic field strength in the range of a few mG and the break energy of the electrons in the order of  $\sim 10^6$ .

We computed the jet power,  $P_{jet}$ , for various particle energy distributions at five different epochs. In the case of broken power-law and PL with  $\gamma_{\rm max}$  models, we find  $P_{\rm iet} \sim 10^{47}$ ergs/sec with a minimum Lorentz factor  $(\gamma_{min})$  set to 10. This value decreases to approximately  $10^{44}$  ergs/sec when  $\gamma_{min}$  is increased to 104. However, for other particle energy distributions with intrinsic curvature, the calculated  $P_{\text{iet}}$  remains around  $10^{44}$  ergs/sec, irrespective of  $\gamma_{min}$ . Interestingly, we found that the estimated  $P_{jet}$  is nearly independent of the bulk Lorentz factor  $(\Gamma)$  and size (R). In the case of intrinsically curved particle energy distributions, such as the log parabola, EDD, and EDA models, the  $P_{\rm jet}$  ( $\approx 10^{44}$  ergs/sec) represents only a small fraction of the Eddington luminosity  $(1.26 \times 10^{47})$ ergs/sec) of the blazar's black hole mass ( $10^9 M_{\odot}$ ; Meyer et al. 2012), suggesting that accretion processes might be driving the jet.

For the source 1ES 0229+200, Acciari et al. (2020) estimated  $P_{\rm jet}$  ( $\approx 10^{44}$  ergs/sec) applying the one zone SSC model assuming a power law with exponential cutoff particle distribution which agrees well with our estimation. Consistent findings have been reported recently by Bora et al. (2024). They calculated the jet power for the HBL source Mrk 501 using the same particle distributions. They found that the

estimated jet power with a broken power-law distribution was around  $10^{47}$  ( $10^{44}$ ) ergs/sec with a minimum electron energy of  $\gamma_{min} = 10$  ( $10^3$ ). However, the estimated jet power was found to be considerably lower than a few times ( $10^{42}$  ergs/sec) for electron energy distributions with intrinsic curvature (such as the log-parabola form).

Correlation studies among the best-fit model parameters provide significant insights regarding the consistency and adequacy of the model in describing the observed broadband SED. For the power-law with a maximum gamma  $(\gamma_{max})$ model, we find a strong anti-correlation between the index p and normalisation N and a positive correlation between index p and magnetic field B. As discussed in Hota et al. (2021), these correlations are against expectations. This is because, in this model, the change in normalization (Equation 6),  $\Delta \mathbb{N}/\mathbb{N} = log(\xi_0^2)\Delta p/2$ , where  $\xi_0^2 \equiv \gamma_0^2 \mathbb{C}$ , occurs for a change in the index,  $\Delta p$ . Since  $\gamma_o$  is much smaller than the  $\gamma$  required to produce X-ray photons,  $log(\xi_0^2)$  should be large; the normalization should vary significantly with a positive correlation when the index changes. However, we find that the normalisation varies with the change in the index with a strong anti-correlation. The observed anti-correlation could be explained by a more sophisticated model in which the acceleration time scale and magnetic field are associated.

We showed that the spectral curvature may also be reproduced by the energy-dependent electron diffusion (EDD) model, where we consider the escape or diffusion time scale to be energy-dependent. As expected by the predictions of the model, we found a strong anti-correlation between the

two model parameter normalization and  $\psi$  with the third parameter  $\kappa$ . The compatibility of the mentioned correlation with the predicted one, for  $\Gamma=20$ , allows us to calculate the reference photon energy  $\xi_R^2=122$  MeV, arising from an electron with energy  $\gamma_R=3.6\times 10^8$ , and the energy of the electrons that are injected into the acceleration region, as  $\gamma_0=3.5\times 10^5$ . Similarly, we consider the spectral curvature may also be reproduced by the energy-dependent electron acceleration (EDA) model, where the acceleration time scale is energy-dependent. For the EDA model, the calculated values are approximate as  $\xi_R^2=66$  MeV,  $\gamma_R=2.66\times 10^8$ , and  $\gamma_0=2\times 10^5$ .

In a previous investigation, Hota et al. (2021) utilized the EDD and EDA models to analyze the X-ray observations of the HBL source, Mkn 421, during its flaring phase, deriving respective spectral parameters. They identified a different range of spectral parameters, with  $\kappa$  falling between 0.3 and 1.0, and  $\psi$  between 1.12 and 1.96. These findings resulted in a slope of  $\log_{10} \xi_R = 0.38$  for the  $\kappa$  vs.  $\log \psi$  anti-correlation. However, in our analysis of EHBL source 1ES 0229+200 (present study), we observe  $\kappa$  and  $\psi$  values within the ranges of 0.11-0.16 and 1.30-1.65, respectively. The correlation between these parameters yields a steeper slope,  $\log_{10} \xi_R =$ 2.54. Consequently, we obtain a significantly higher value of  $\xi_R^2$  (10<sup>4</sup> times larger than the HBL source). Notably, the calculated values of  $\xi_R^2$  in both the EDD and EDA models predominantly fall within the MeV range, surpassing the Synchrotron spectral energy range under consideration. This suggests favourable conditions for these models to fit the broadband spectrum of EHBL sources effectively. In contrast, for Mkn 421 during its flaring phase, the corresponding photon energy ( $\xi_R^2 \sim 5.6 \text{ keV}$ ) remains within the considered energy range (0.5 -18 keV) in both the EDD and EDA models, contradicting the spectral fitting of HBL sources with these models. Additionally, we get a relationship  $\gamma_0 = 9.6$  $\times$  10<sup>-04</sup>  $\gamma_R$  when fitting the correlation between  $\kappa$  and  $\ln \mathbb{N}$ , which is more likely appropriate in the physical framework than it is observed for the HBL source (i.e  $\gamma_0 \sim 0.2 \gamma_R$ ) (Hota et al. 2021). Moreover, we can now get the actual values of  $\gamma_R$  and, more importantly,  $\gamma_0$  while using the SSC model (current study).

The intrinsically curved particle distribution models (EDD and EDA models) considered in this work are simple and have

analytical solutions; the physical situation may really be more complicated. Furthermore, considering both escape and acceleration time scales to be energy-dependent would be more physically plausible. Compared to the power-law form used in this work, the energy dependency of various time scales may differ. Eventually, in order to provide a more complete picture, the analysis must be expanded to include some other EHBL blazars. Moving forward, it would be valuable to explore additional aspects, such as temporal variations and extended datasets, to further refine our understanding of the jet dynamics and uncover any nuanced behaviours that might emerge over an extended observation period. Additionally, comparative analyses with other blazar sources could provide a comprehensive perspective on the universality of the observed trends in jet power and its dependence on particle energy distributions.

#### **ACKNOWLEDGEMENTS**

We thank the anonymous referee for insightful comments and constructive suggestions. The authors JH and ACP would like to acknowledge Inter-University Centre for Astronomy and Astrophysics (IUCAA), Pune, India, for providing facilities to carry out this work. This publication uses data from the Astrosat mission of the Indian Space Research Organisation(ISRO), archived at the Indian Space Science Data Centre(ISSDC). This work has used the data from the Soft X-ray Telescope (SXT) developed at TIFR, Mumbai. Laxpc-Soft software is used for analysis of the LAXPC data and we acknowledge the LAXPC Payload Operation Center (TIFR, Mumbai). This research has made use of data, software and/or web tools obtained from the High Energy Astrophysics Science Archive Research Center (HEASARC), a service of the Astrophysics Science Division at NASA/GSFC and of the Smithsonian Astrophysical Observatory's High Energy Astrophysics Division.

Facilities: Fermi(LAT), AstroSat (UVIT, SXT AND LAXPC), Swift(UVOT)

Software: fermipy-v0.17.4 (Fermipywebpage:https://fermipy.readthedocs.io/en/latest/),

XSPEC (https://heasarc.gsfc.nasa.gov/xanadu/xspec/), HEASARC(https://heasarc.gsfc.nasa.gov/docs/software/heasoft/)

## **REFERENCES**

Abdo, A. A., Ackermann, M., Ajello, M., et al. 2011, The

Astrophysical Journal, 736, 131,

doi: 10.1088/0004-637x/736/2/131

Abdollahi, S., Acero, F., Ackermann, M., et al. 2020, The Astrophysical Journal Supplement Series, 247, 33,

doi: 10.3847/1538-4365/ab6bcb

Acciari, V. A., Ansoldi, S., Antonelli, L. A., et al. 2020, ApJS, 247,

16, doi: 10.3847/1538-4365/ab5b98

- Acciari, V. A., Agudo, I., Aniello, T., et al. 2023, A&A, 670, A145, doi: 10.1051/0004-6361/202244126
- Acero, F., Ackermann, M., Ajello, M., et al. 2015, ApJS, 218, 23, doi: 10.1088/0067-0049/218/2/23
- Ackermann, M., Ajello, M., Allafort, A., et al. 2011, ApJ, 743, 171, doi: 10.1088/0004-637X/743/2/171
- Agrawal, P. 2006, Advances in Space Research, 38, 2989, doi: https://doi.org/10.1016/j.asr.2006.03.038
- Agrawal, P. C., Yadav, J. S., Antia, H. M., et al. 2017, Journal of Astrophysics and Astronomy, 38, 30, doi: 10.1007/s12036-017-9451-z
- Aguilar-Ruiz, E., Fraija, N., Galván-Gámez, A., & Benítez, E. 2022, MNRAS, 512, 1557, doi: 10.1093/mnras/stac591
- Aharonian, F., Akhperjanian, A. G., Bazer-Bachi, A. R., et al. 2007a, ApJL, 664, L71, doi: 10.1086/520635
- Aharonian, F., Akhperjanian, A. G., Barres de Almeida, U., et al. 2007b, A&A, 475, L9, doi: 10.1051/0004-6361:20078462
- Aleksić, J., Alvarez, E. A., Antonelli, L. A., et al. 2012, A&A, 542, A100, doi: 10.1051/0004-6361/201117442
- Aliu, E., Archambault, S., Arlen, T., et al. 2014, ApJ, 782, 13, doi: 10.1088/0004-637X/782/1/13
- Antia, H. M., Yadav, J. S., Agrawal, P. C., et al. 2017, ApJS, 231, 10, doi: 10.3847/1538-4365/aa7a0e
- Arnaud, K. A. 1996, Astronomical Society of the Pacific Conference Series, Vol. 101, XSPEC: The First Ten Years (George H. Jacoby and Jeannette Barnes), 17
- Atwood, W. B., Abdo, A. A., Ackermann, M., et al. 2009, ApJ, 697, 1071, doi: 10.1088/0004-637X/697/2/1071
- Begelman, M. C., Blandford, R. D., & Rees, M. J. 1984, Rev. Mod. Phys., 56, 255, doi: 10.1103/RevModPhys.56.255
- Begelman, M. C., Sikora, M., Giommi, P., et al. 1987, ApJ, 322, 650, doi: 10.1086/165760
- Bertin, E., & Arnouts, S. 1996, A&AS, 117, 393, doi: 10.1051/aas:1996164
- Biteau, J., Prandini, E., Costamante, L., et al. 2020, Nature Astronomy, 4, 124, doi: 10.1038/s41550-019-0988-4
- Blandford, R., Meier, D., & Readhead, A. 2019, Annual Review of Astronomy and Astrophysics, 57, 467,
- doi: 10.1146/annurev-astro-081817-051948
- Blandford, R. D., & Levinson, A. 1995, ApJ, 441, 79, doi: 10.1086/175338
- Blandford, R. D., & Payne, D. G. 1982, MNRAS, 199, 883, doi: 10.1093/mnras/199.4.883
- Blandford, R. D., & Znajek, R. L. 1977, MNRAS, 179, 433, doi: 10.1093/mnras/179.3.433
- B lażejowski, M., Sikora, M., Moderski, R., & Madejski, G. M. 2000, ApJ, 545, 107, doi: 10.1086/317791
- Bloom, S. D., & Marscher, A. P. 1996, ApJ, 461, 657, doi: 10.1086/177092

- Bora, H., Khatoon, R., Misra, R., & Gogoi, R. 2024, MNRAS, doi: 10.1093/mnras/stae706
- Breeveld, A. A., Landsman, W., Holland, S. T., et al. 2011, in American Institute of Physics Conference Series, Vol. 1358,
  Gamma Ray Bursts 2010, ed. J. E. McEnery, J. L. Racusin, & N. Gehrels, 373–376, doi: 10.1063/1.3621807
- Celotti, A., & Ghisellini, G. 2008, MNRAS, 385, 283, doi: 10.1111/j.1365-2966.2007.12758.x
- Costamante, L., Bonnoli, G., Tavecchio, F., et al. 2018, Monthly Notices of the Royal Astronomical Society, 477, 4257, doi: 10.1093/mnras/sty857
- Costamante, L., Bonnoli, G., Tavecchio, F., et al. 2018, MNRAS, 477, 4257, doi: 10.1093/mnras/sty857
- Costamante, L., Ghisellini, G., Giommi, P., et al. 2001, A&A, 371, 512, doi: 10.1051/0004-6361:20010412
- Dermer, C. D., Schlickeiser, R., & Mastichiadis, A. 1992, A&A, 256, L27
- Diwan, R., Prince, R., Agarwal, A., et al. 2023, MNRAS, 524, 4333, doi: 10.1093/mnras/stad2088
- Elvis, M., Plummer, D., Schachter, J., & Fabbiano, G. 1992, ApJS, 80, 257, doi: 10.1086/191665
- Fan, J.-H., Yuan, Y.-H., Liu, Y., et al. 2008, Publications of the Astronomical Society of Japan, 60, 707, doi: 10.1093/pasj/60.4.707
- Foffano, L., Prandini, E., Franceschini, A., & Paiano, S. 2019, MNRAS, 486, 1741, doi: 10.1093/mnras/stz812
- Foffano, L., Prandini, E., Franceschini, A., & Paiano, S. 2019, Monthly Notices of the Royal Astronomical Society, 486, 1741, doi: 10.1093/mnras/stz812
- Fossati, G., Maraschi, L., Celotti, A., Comastri, A., & Ghisellini, G. 1998, MNRAS, 299, 433, doi: 10.1046/j.1365-8711.1998.01828.x
- Franceschini, A., Rodighiero, G., & Vaccari, M. 2008, A&A, 487, 837, doi: 10.1051/0004-6361:200809691
- Ghisellini, G., Maraschi, L., & Treves, A. 1985, A&A, 146, 204Ghisellini, G., Padovani, P., Celotti, A., & Maraschi, L. 1993, ApJ, 407, 65, doi: 10.1086/172493
- Ghisellini, G., Righi, C., Costamante, L., & Tavecchio, F. 2017, MNRAS, 469, 255, doi: 10.1093/mnras/stx806
- Ghisellini, G., & Tavecchio, F. 2008, MNRAS, 387, 1669, doi: 10.1111/j.1365-2966.2008.13360.x
- Giommi, P., Blustin, A. J., Capalbi, M., et al. 2006, A&A, 456, 911, doi: 10.1051/0004-6361:20064874
- Goswami, P., Sahayanathan, S., Sinha, A., Misra, R., & Gogoi, R. 2018, MNRAS, 480, 2046, doi: 10.1093/mnras/sty2003
- Goswami, P., Zacharias, M., Zech, A., et al. 2024, A&A, 682, A134, doi: 10.1051/0004-6361/202348121
- Hota, J., Shah, Z., Khatoon, R., et al. 2021, MNRAS, 508, 5921, doi: 10.1093/mnras/stab2903

- Jones, T. W., O'Dell, S. L., & Stein, W. A. 1974, ApJ, 188, 353, doi: 10.1086/152724
- Kalberla, P. M. W., Burton, W. B., Hartmann, D., et al. 2005, A&A, 440, 775, doi: 10.1051/0004-6361:20041864
- Kaufmann, S., Wagner, S. J., Tibolla, O., & Hauser, M. 2011, A&A, 534, A130, doi: 10.1051/0004-6361/201117215
- Khatoon, R., Shah, Z., Hota, J., et al. 2022, MNRAS, 515, 3749, doi: 10.1093/mnras/stac1964
- Kneiske, T. M., & Dole, H. 2010, A&A, 515, A19, doi: 10.1051/0004-6361/200912000
- Li, W.-J., Xue, R., Long, G.-B., et al. 2022, A&A, 659, A184, doi: 10.1051/0004-6361/202142051
- MAGIC Collaboration, Acciari, V. A., Ansoldi, S., et al. 2019a, MNRAS, 490, 2284, doi: 10.1093/mnras/stz2725
- —. 2020, A&A, 640, A132, doi: 10.1051/0004-6361/202037811
- MAGIC Collaboration, Ahnen, M. L., Ansoldi, S., Antonelli, L. A., et al. 2018, A&A, 620, A181,
  - doi: 10.1051/0004-6361/201833704
- MAGIC Collaboration, Acciari, V. A., Ansoldi, S., Antonelli, L. A., et al. 2019b, MNRAS, 486, 4233, doi: 10.1093/mnras/stz943
- Mannheim, K., & Biermann, P. L. 1992, A&A, 253, L21
- Maraschi, L., Ghisellini, G., & Celotti, A. 1992, ApJL, 397, L5, doi: 10.1086/186531
- Massaro, E., Perri, M., Giommi, P., & Nesci, R. 2004, A&A, 413, 489, doi: 10.1051/0004-6361:20031558
- Mattox, J. R., Bertsch, D. L., Chiang, J., et al. 1996, ApJ, 461, 396, doi: 10.1086/177068
- Meyer, M., Raue, M., Mazin, D., & Horns, D. 2012, A&A, 542, A59, doi: 10.1051/0004-6361/201118284
- Misra, R., Roy, J., & Yadav, J. S. 2021, arXiv e-prints, arXiv:2102.06402. https://arxiv.org/abs/2102.06402
- Misra, R., Yadav, J. S., Chauhan, J. V., et al. 2017, The Astrophysical Journal, 835, 195, doi: 10.3847/1538-4357/835/2/195
- Mücke, A., & Protheroe, R. J. 2001, Astroparticle Physics, 15, 121, doi: 10.1016/S0927-6505(00)00141-9
- Neronov, A., & Vovk, I. 2010, Science, 328, 73, doi: 10.1126/science.1184192
- Padovani, P., & Giommi, P. 1995, ApJ, 444, 567, doi: 10.1086/175631
- Pian, E., Vacanti, G., Tagliaferri, G., et al. 1997, The Astrophysical Journal, 492, L17, doi: 10.1086/311083
- Postma, J. E., & Leahy, D. 2017, PASP, 129, 115002, doi: 10.1088/1538-3873/aa8800
- Prandini, E., Arcaro, C. H. E., Asano, K., et al. 2019, in International Cosmic Ray Conference, Vol. 36, 36th International Cosmic Ray Conference (ICRC2019), 768, doi: 10.22323/1.358.0768

- Rao, A. R., Bhattacharya, D., Bhalerao, V. B., Vadawale, S. V., & Sreekumar, S. 2017, arXiv e-prints, arXiv:1710.10773. https://arxiv.org/abs/1710.10773
- Rao, A. R., Singh, K. P., & Bhattacharya, D. 2016, arXiv e-prints, arXiv:1608.06051. https://arxiv.org/abs/1608.06051
- Roming, P. W. A., Kennedy, T. E., Mason, K. O., et al. 2005, SSRv, 120, 95, doi: 10.1007/s11214-005-5095-4
- Rybicki, G. B., & Lightman, A. P. 1986, Radiative Processes in Astrophysics (Wiley-VCH)
- Sambruna, R. M. 2000, AIP Conference Proceedings, 515, 19, doi: 10.1063/1.1291340
- Schlafly, E. F., & Finkbeiner, D. P. 2011, The Astrophysical Journal, 737, 103, doi: 10.1088/0004-637X/737/2/103
- Shah, Z., Sahayanathan, S., Mankuzhiyil, N., et al. 2017, MNRAS, 470, 3283, doi: 10.1093/mnras/stx1194
- Sikora, M., Begelman, M. C., & Rees, M. J. 1994, ApJ, 421, 153, doi: 10.1086/173633
- Singh, K., Stewart, G., Westergaard, N., et al. 2017, Journal of Astrophysics and Astronomy, 38, doi: 10.1007/s12036-017-9448-7
- Singh, K. P., Tandon, S. N., Agrawal, P. C., et al. 2014, in SPIE,
  Vol. 9144, Space Telescopes and Instrumentation 2014:
  Ultraviolet to Gamma Ray, ed. T. Takahashi, J.-W. A. den
  Herder, & M. Bautz, International Society for Optics and
  Photonics (SPIE), 517 531, doi: 10.1117/12.2062667
- Singh, K. P., Stewart, G. C., Chandra, S., et al. 2016, in Society of Photo-Optical Instrumentation Engineers (SPIE) Conference Series, Vol. 9905, Proc. SPIE, 99051E, doi: 10.1117/12.2235309
- Singh, K. P., Stewart, G. C., Westergaard, N. J., et al. 2017, Journal of Astrophysics and Astronomy, 38, 29, doi: 10.1007/s12036-017-9448-7
- Sinha, A., Sahayanathan, S., Acharya, B. S., et al. 2017, ApJ, 836, 83, doi: 10.3847/1538-4357/836/1/83
- Sokolov, A., Marscher, A. P., & McHardy, I. M. 2004, The Astrophysical Journal, 613, 725, doi: 10.1086/423165
- Tanaka, Y. T., Stawarz, L., Finke, J., et al. 2014, ApJ, 787, 155, doi: 10.1088/0004-637X/787/2/155
- Tandon, S. N., Hutchings, J. B., Ghosh, S. K., et al. 2017a, Journal of Astrophysics and Astronomy, 38, 28, doi: 10.1007/s12036-017-9445-x
- Tandon, S. N., Subramaniam, A., Girish, V., et al. 2017b, AJ, 154, 128, doi: 10.3847/1538-3881/aa8451
- Tavecchio, F., Ghisellini, G., Foschini, L., et al. 2010, MNRAS, 406, L70, doi: 10.1111/j.1745-3933.2010.00884.x
- Tavecchio, F., Ghisellini, G., Ghirlanda, G., Costamante, L., & Franceschini, A. 2009, MNRAS, 399, L59, doi: 10.1111/j.1745-3933.2009.00724.x
- Tramacere, A., Massaro, F., & Cavaliere, A. 2007, A&A, 466, 521, doi: 10.1051/0004-6361:20066723

- Urry, C. M., & Mushotzky, R. F. 1982, ApJ, 253, 38, doi: 10.1086/159607
- Urry, C. M., & Padovani, P. 1995, Publications of the Astronomical Society of the Pacific, 107, 803, doi: 10.1086/133630
- Vovk, I., Taylor, A. M., Semikoz, D., & Neronov, A. 2012, ApJL, 747, L14, doi: 10.1088/2041-8205/747/1/L14
- Wilms, J., Allen, A., & McCray, R. 2000, ApJ, 542, 914, doi: 10.1086/317016
- Woo, J.-H., Urry, C. M., van der Marel, R. P., Lira, P., & Maza, J. 2005, ApJ, 631, 762, doi: 10.1086/432681
- Xue, R., Liu, R.-Y., Wang, X.-Y., Yan, H., & Böttcher, M. 2019, ApJ, 871, 81, doi: 10.3847/1538-4357/aaf720
- Yadav, J. S., Agrawal, P. C., Antia, H. M., et al. 2016, in Society of Photo-Optical Instrumentation Engineers (SPIE) Conference Series, Vol. 9905, Proc. SPIE, 99051D, doi: 10.1117/12.2231857

- Yadav, J. S., Agrawal, P. C., Antia, H. M., et al. 2016, in SPIE, Vol. 9905, Space Telescopes and Instrumentation 2016: Ultraviolet to Gamma Ray, ed. J.-W. A. den Herder, T. Takahashi, & M. Bautz, International Society for Optics and Photonics (SPIE), 374 388, doi: 10.1117/12.2231857
- Zdziarski, A. A., & Bottcher, M. 2015, MNRAS, 450, L21, doi: 10.1093/mnrasl/slv039
- Zech, A., & Lemoine, M. 2021, A&A, 654, A96, doi: 10.1051/0004-6361/202141062
- Zhang, L., Liu, Y., & Fan, J. 2022, ApJ, 935, 4, doi: 10.3847/1538-4357/ac7bde